JCBFM

A novel molecular magnetic resonance imaging agent targeting activated leukocyte cell adhesion molecule as demonstrated in mouse brain metastasis models

Niloufar Zarghami[1] , Manuel Sarmiento Soto[1],
Francisco Perez-Balderas[1], Alexandre A Khrapitchev[1] ,
Christina Simoglou Karali[1], Vanessa A Johanssen[1],
Olaf Ansorge[2], James R Larkin[1] and Nicola R Sibson[1]

Abstract

Molecular magnetic resonance imaging (MRI) allows visualization of biological processes at the molecular level. Upregulation of endothelial ALCAM (activated leukocyte cell adhesion molecule) is a key element for leukocyte recruitment in neurological disease. The aim of this study, therefore, was to develop a novel molecular MRI contrast agent, by conjugating anti-ALCAM antibodies to microparticles of iron oxide (MPIO), for detection of endothelial ALCAM expression *in vivo*. Binding specificity of ALCAM-MPIO was demonstrated *in vitro* under static and flow conditions. Subsequently, in a proof-of-concept study, mouse models of brain metastasis were induced by intracardial injection of brain-tropic human breast carcinoma, lung adenocarcinoma or melanoma cells to upregulate endothelial ALCAM. At selected time-points, mice were injected intravenously with ALCAM-MPIO, and ALCAM-MPIO induced hypointensities were observed on T_2*-weighted images in all three models. Post-gadolinium MRI confirmed an intact blood-brain barrier, indicating endoluminal binding. Correlation between endothelial ALCAM expression and ALCAM-MPIO binding was confirmed histologically. Statistical analysis indicated high sensitivity (80–90%) and specificity (79–83%) for detection of endothelial ALCAM *in vivo* with ALCAM-MPIO. Given reports of endothelial ALCAM upregulation in numerous neurological diseases, this advance in our ability to image ALCAM *in vivo* may yield substantial improvements for both diagnosis and targeted therapy.

Introduction

Immune activation and inflammation within the brain is a classical feature of a spectrum of acute and chronic neurological diseases, including ischemia, immune-mediated disorders (e.g. multiple sclerosis), neurodegenerative diseases (e.g. Alzheimer's and Parkinson's diseases), infection, trauma and cancer.[1] As part of the inflammatory response, expression of cell adhesion molecules (CAMs) on the cerebrovascular endothelium

[1]Cancer Research UK and Medical Research Council Oxford Institute for Radiation Oncology, Department of Oncology, University of Oxford, Oxford, UK
[2]Department of Clinical Neuropathology, John Radcliffe Hospital, Oxford, UK

Corresponding author:
Nicola R Sibson, Department of Oncology, Old Road Campus Research Building, University of Oxford, Oxford OX3 7LJ, UK.
Email: nicola.sibson@oncology.ox.ac.uk

is upregulated, and these mediate recruitment of immune cells to the inflammatory foci. Different CAMs mediate each step, and the correct molecules must interact within a short period of time for successful leukocyte recruitment.[2]

Advances in science and technology in the last few decades have allowed identification of CAMs that can provide important information about the molecular and cellular processes involved in various stages of neuroinflammation. These biomarkers, which are expressed at an abnormal level during disease progression, can be useful both for initial diagnosis and to shed light on prognosis. We have previously demonstrated that endoluminal CAMs yield an accessible 'tag' for targeted molecular imaging agents to bind to without the need to cross the BBB, and such agents have been developed extensively in experimental models of diseases with a neuro-inflammatory component.[3,4] Vascular cell adhesion molecule 1 (VCAM-1), inducible cell adhesion molecule 1 (ICAM-1), and P-selectin have been the most popular inflammation biomarkers in animal models of neurological disease to date, including models of stroke, Alzheimer's disease and multiple sclerosis.[5–10] These inflammatory markers have the advantage of being selectively expressed on the lumen of vessels, allowing molecularly targeted microparticles of iron oxide (MPIO) to adhere to the site of upregulation without the need to cross the BBB. Moreover, antibody conjugated MPIO have been shown to provide a combination of high payload of contrast, combined with rapid blood clearance (1.2 min), resulting in a high degree of specificity and sensitivity for target detection in vivo.[11]

Activated leukocyte cell adhesion molecule (ALCAM, CD166), another member of CAMs family, has been shown to specifically localise at the intercellular junctions between endothelial cells, and is thought to play a pivotal role in the machinery of diapedesis and extravasation of T cells.[12] Although early studies of ALCAM date back some 20 years, it is only recently that attention has focused on the role of endothelial ALCAM in leukocyte trafficking in response to neurological diseases such as multiple sclerosis (MS).[13–15] In particular, a very recent study by Michel et al, provides evidence for ALCAM involvement in B cell migration into the central nervous system.[16] Further, ALCAM has been suggested to play a role in the integrity of the blood-brain barrier (BBB), with ALCAM knockout (KO) mice developing severe experimental autoimmune encephalomyelitis (EAE) owing to increased permeability of the BBB.[15] Very recently, we and others have demonstrated that ALCAM is specifically and selectively upregulated on cerebral vessels that are closely associated with both breast cancer brain metastases[17] and lung cancer brain metastases,[18] and that inhibiting tumour-endothelial ALCAM interactions reduces tumour seeding to the brain. It is becoming clear, therefore, that ALCAM is a key component of the inflammatory response in the brain and, importantly, in the recruitment of leukocytes to sites of disease and injury.

On the basis of these studies, highlighting ALCAM as a potential vascular target in multiple neurological diseases, we hypothesised that ALCAM might provide a new and sensitive target for both identifying early neurological disease and enabling stratification of patients to specific treatments. In this work, therefore, we have developed, validated and implemented a novel molecular MRI contrast agent using MPIO conjugated with anti-ALCAM antibodies. Binding efficacy of this novel ALCAM targeted agent (ALCAM-MPIO) was validated firstly in vitro and, secondly, in vivo, using three different models of brain metastasis for this proof-of-concept study.

MATERIALS and METHODS

ALCAM-MPIO synthesis

Three different primary antibodies against mouse ALCAM were evaluated: (1) R&D systems, (cat. no. MAB1172), (2) LifeSpan Biosciences, Inc. (cat. no. LS-C292613), and (3) eBioscience^{TM} Fisher Scientific (cat. no. 1401661-82). To construct ALCAM-MPIO, antibodies were conjugated to ProMag^{TM} carboxylic MPIO (0.76 μm diameter, 2.114 x 10^9 particles/mg bead, iron content: 26%; cat. no. PMC1N, Bangs Laboratory Inc., USA), as described previously.[11] As a control, MPIO were conjugated with rat anti-mouse IgG1 antibody, (low endotoxin/azide-free, cat. no. 0116-14; Cambridge Bioscience). The number of antibodies (ALCAM or IgG) loaded on the MPIO was measured using a BD FACS-Calibur flow cytometer, on channel FL4 (661/16 nm band pass filter), as described previously.[11,19] Antibody loading was determined against a standard calibration curve using Quantum Alexa Fluor 647 MESF (Bangs Laboratory Inc., USA).

ALCAM-MPIO binding in vitro under static and flow conditions

First, mouse endothelial (sEnd-1) and human brain endothelial cells (hCMEC/D3) were treated with IL-Interleukin 1 beta (IL-1b; Pepro EC, UK) or tumor necrosis factor (TNF; Peprotech EC, UK) for 20 hours (10 ng/ml and 50 ng/ml) to assess ALCAM upregulation in response to the inflammatory stimuli (Supplementary Methods). Next, ALCAM-MPIO binding was assessed under static conditions to sEnd-

1 cells stimulated with TNF, as described in Supplementary Methods. Cells were subsequently immunostained for ALCAM, and MPIO stained with an appropriate Texas Red antibody (Supplementary Methods). Fluorescent images were taken using a Leica SP8 (Germany) and the percentage of co-localized red (MPIO) and green (ALCAM) pixels were calculated for each field-of-view (FoV). The ALCAM antibody showing the highest MPIO loading and static binding was chosen for the subsequent *in vitro* flow experiment and *in vivo* study. Specific binding of fluorescently labeled ALCAM/IgG-MPIO was assessed under flow conditions in glass capillaries coated with recombinant mouse ALCAM protein or as a control condition with bovine serum albumin (BSA) (Supplementary Methods). Images were acquired across 10 separate FoV along the capillaries using X40 magnification and the FITC channel, and the number of bound ALCAM- or IgG-MPIO per FoV were counted.

Tumor cells

For the proof-of-principle *in vivo* imaging of ALCAM, three mouse models of brain metastasis were studied in which three brain tropic human-derived tumor cell lines were used, as described previously:[20] (i) breast carcinoma MDA231Br-GFP cells (kind gift from Dr. P. Steeg, USA); (ii) melanoma H1_DL2 cells (kind gift from Prof. F. Thorsen, Norway); and (iii) lung adeno-carcinoma SEBTA-001 cells (kind gift from Prof. G. Pilkington, UK). Details of cell culture can be found in Supplementary Methods.

Mouse brain metastasis models

All animal experiments were approved by the University of Oxford Clinical Medicine Ethics Review Committee and the UK Home Office (Animals [Scientific Procedures] Act 1986), and conducted in accordance with the University of Oxford Policy on the Use of Animals in Scientific Research, the ARRIVE Guidelines and Guidelines for the Welfare and Use of Animals in Cancer Research.[21] Female SCID mice (7–8 weeks; Charles River, Kent, UK) were anaesthetised with 2–3% (vol/vol) isoflurane in oxygen and injected via the left cardiac ventricle under ultrasound guidance (Vevo 3100 Imaging System; Fujifilm VisualSonics) with 1×10^5 tumor cells in 100 µl of sterile phosphate buffered saline (PBS).[17,20,22] To assess ALCAM upregulation on metastasis-associated vessels during micrometastatic growth, mice (n = 4 per time-point) were perfused on day 7, 14, 21 or 28 after tumor injection for the breast cancer and melanoma brain metastasis models. Two

later time-points were assessed for the lung cancer brain metastasis model, days 35 and 42, owing to the slow doubling time and, hence, tumor growth rate of the SEBTA-001 cell line.[20,23] All mice were transcardially perfusion-fixed under terminal anaesthesia, using 0.9% heparinized saline followed by periodate-lysine-paraformaldehyde (PLP) containing 0.1% glutaraldehyde (PLP$_{light}$).

Immunohistochemistry and immunofluorescence; mouse tissue

ALCAM upregulation was assessed immunohistochemically on mouse brain sections as described in Supplementary Methods. Histological slides were digitally scanned on an Aperio Brightfield scanner (Leica Biosystems) at X20 magnification and analyzed using Imagescope (Leica Biosystems) software. Over 30 tumor sections were analyzed for each model at each time-point. Naïve mouse brain was also stained for ALCAM to assess background levels of this marker. The presence of ALCAM on cerebral vessels was assessed by immunofluorescent co-localization staining of ALCAM and endothelial cells (CD31) (see Supplementary Methods). Images were acquired using an inverted confocal microscope (LSM-780; Carl Zeiss Microimaging) and analyzed using Zen software (Carl Zeiss). Co-localization analysis between ALCAM and CD31 was performed using an in-house plugin for Fiji open-source software, which measured the percentage of overlapped area for the two markers above a user set threshold for each signal.

In vivo brain imaging

To demonstrate efficacy of ALCAM-MPIO imaging *in vivo*, days 21 and 28 after tumor cell injection were chosen for the breast and melanoma brain metastasis models, based on previous studies showing that these tumors are still in the micrometastatic stage and that the BBB is intact up to day 28.[20,22] A single time-point, day 42, was used for the lung brain metastasis model, owing to the slower growth rate. On the day of imaging, tumor-bearing mice were injected intravenously with either ALCAM-MPIO or control IgG-MPIO (4 mg iron/Kg). Moreover, to confirm the specific binding of ALCAM-MPIO in tumour models, naïve mice (n = 2/group) were injected with either (i) untargeted MPIO, (ii) IgG-MPIO or (iii) ALCAM-MPIO (all at the same dose of 4 mg iron/Kg body weight in 100 µl PBS).

All MRI experiments were performed using a 7.0 T horizontal bore MRI spectrometer equipped with DDR console running Agilent VnmrJ 4.2 software (Agilent Technologies Inc., Santa Clara, USA). Mice

were anaesthetized with 2–3% v/v isoflurane in a mixture of 90% air:10% oxygen. All iron oxide contrast agents were injected intravenously, via ~ 1 m of tubing (0.28 mm ID, Smiths Medical[TM]) attached to a butterfly cannula (30 G insulin syringe) inserted into a tail vein, whilst the mice were outside the magnetic field. Mice were placed prone in a customised 3 D printed cradle, with the head fixed using cheek pads, and positioned inside a 26 mm internal diameter transmit/receive birdcage RF coil (Rapid Biomedical, Rimpar, Germany). Anaesthesia was maintained throughout MRI at 1.5–2% v/v isoflurane in 90% air:10% oxygen, and respiration monitored via a pressure balloon in contact with the chest. Core temperature was monitored using an optical rectal temperature probe and maintained at $37 \pm 0.5\,°C$.[24] The coil was positioned within the magnet and shimming performed using a point resolved spectroscopy sequence (PRESS), with an excitation voxel covering the mouse brain. The zero and the first order shims were adjusted manually until the spectral linewidth was 20–30 Hz full width at half maximum (FWHM). After a 30 min warm up scan to bring the gradient coils to constant temperature, mice were imaged with a 3 D T_2*-weighted multigradient echo (MGE3D) sequence[11] (start of scan $= 40 \pm 0.5$ min after MPIO injection): excitation angle $= 15°$; repetition time (TR) $= 48.8$ ms; time of the 1st echo $(TE_1) = 4$ ms; echo separation time $(TE_2) = 7$ ms; number of echoes $= 6$; SW $= 50$ kHz; FoV $= 22.5 \times 22.5 \times 22.5$ mm^3; acquisition matrix $= 256 \times 192 \times 192$ (images zero-filled to $256 \times 256 \times 256$; final isotropic resolution $= 88\,\mu m$); single average (NT $= 1$) and total acquisition time ~ 30 min. T_2*-weighted MGE3D images were reconstructed using a home-built MATLAB (Mathworks) program based on the square root of the sum of squares (SqrtSOS) of individual echoes algorithm, as described previously.[11] T_1-weighted spin-echo datasets were also acquired pre- and 5 min post-gadolinium-DTPA injection (30 μl i.v.; Omniscan, GE Healthcare), to assess BBB permeability: TR $= 500$ ms; TE $= 10$ ms; average $= 1$; FoV $= 22.5 \times 22.5$ mm^2; acquisition matrix $= 192 \times 192$ (zero-filled to 256×256); slice thickness $= 0.7$ mm; single average (NT $= 1$) and total acquisition time ~ 1.6 min.

Image processing and analyses

All T_2*-weighted images presented are SqrtSOS of all echoes from the T_2*weighted MGE3D datasets. Cerebral structures for each T_2*-weighted MGE3D dataset were manually segmented using ITK-SNAP (itksnap.org) 3 D balloon force option.[25] Subsequently, automated image processing of segmented images were performed using an in-house MATLAB code.[20,22,26]

The signal intensity of each individual voxel was statistically compared with the intensity distribution of all surrounding voxels within a 5 x 5 x 5 (voxel) volume, to determine whether it was significantly lower than the average local signal intensity. To segment true hypointense voxels arising from bound MPIO, a threshold value was set at a fraction of the local mean signal intensity (0.68 times less than the mean value), as optimized and described previously.[22,26] Below this threshold, voxels were designated as MPIO-induced hypointensities. Natural hypointense signals from ventricles and sinuses were excluded by using an upper threshold limit of 20 contiguous hypointense voxels (≥ 20), and single voxel hypointensities were excluded as noise. All datasets were analysed blind to the experimental cohort with regards to the initial segmentation of the brain, and all subsequent analysis was automated and, thus, performed blind.

MRI and histology co-registration

Every other histological section (10 μm) through the brain was stained for ALCAM, and tumours delineated manually using Imagescope software; day 21 for MDA231Br-GFP and H1_DL2 models, and day 42 for the SEBTA-001 model. Subsequently, for each MRI slice in the 3 D dataset, five stained histological sections were identified that spanned the thickness of the MRI slice ($\sim 88\,\mu m$, accounting for 20% shrinkage during perfusion-fixation and the gap between stained sections), as shown in Supplemental Figure S1. Tumour volume was calculated by adding the tumour areas (μm^2) on each stained histological section multiplied by slice thickness (10 μm), with linear interpolation across the unstained alternate sections.

The anatomical location of each metastasis identified histologically was visually matched with hypointensities on the MRI slices, using anatomical cues to determine spatial correspondence. It should be noted, that since the MPIO are known to induce a contrast effect approximately 50x their diameter, it is impossible to determine absolute spatial location of an MPIO from its contrast effect. Indeed, where more than one MPIO is bound, this absolute localisation is further confounded. Thus, close correspondence of hypointensities and metastases relative to anatomical markers was considered to indicate a positive result. Spatial correlation between histology and MRI was assessed blind by two independent observers, and co-registration between metastases and hypointensities only considered positive when both observers agreed.

Immunohistochemistry; human tissue

Expression of ALCAM was assessed in human brain metastasis biopsies from breast, melanoma and lung adenocarcinoma. All human samples were obtained from the Oxford Brain Bank, licensed by the Human Tissue Authority and operating under generic Research Ethics Committee approval (Reference 15/SC/0639). Paraffin-embedded human brain metastasis sections were stained for ALCAM and CD34 (marker of endothelial cells) using anti-human ALCAM and CD34 antibodies, as described in Supplementary Methods, and counterstained with cresyl violet.

Statistical analysis

Statistical analyses were performed using Prism (GraphPad Software, San Diego, CA, USA). Parametric analyses of variance (ANOVA) was applied after assessing normality of variables using the Shapiro-Wilk test. Tukey post-hoc tests were conducted to identify significant differences between groups. All error bars are shown as mean ± standard deviation (SD).

Classification performance of ALCAM-MPIO MRI for identifying metastases was assessed by manually classifying each tumour as positive for endothelial ALCAM histologically (±ALCAM), then identifying the same location in the MRI, as described above and confirming whether the tumour location had a visible hypointensity. These classification results were used to construct 2x2 contingency tables where all tumours were classified as ±ALCAM histology and ±MRI hypointensity. From the 2×2 tables, the following classification metrics were calculated: sensitivity (the chance of a histologically ALCAM positive tumour being identified by ALCAM-MRI), specificity (the chance of an MRI negative tumour also being histologically ALCAM negative), accuracy (the overall chance of MRI classification matching histological classification), prevalence (the overall chance of a tumour being histologically ALCAM positive) and positive predictive value (PPV, the chance of an MRI-detected tumour being histologically ALCAM positive). Fisher's exact statistics was determined for each table where

$$p = \frac{(TP+FP)! * (FN+TN)! * (TP+FN)! * (FP+TN)! *}{TP! * TN! * FP! * FN! * \sum(TP,FP,TN,FN)!}.$$

TP = true positive, TN = true negative, FP = false positive, FN = false negative. This statistic gives the p value for the probability that the given classification did not arise randomly, i.e. a significant Fisher's exact test indicates that the classification is performing significantly better than chance.

Results

Optimization and binding assessment of ALCAM-MPIO conjugate

ALCAM immunocytochemistry showed upregulation of this marker on both mouse and human endothelial cell lines treated with IL-1β or TNF, at both doses tested (10 ng/ml and 50 ng/ml) (Supplemental Figure S2). Low expression of ALCAM was detected on untreated endothelial cells, and no signal was detected for the ALCAM negative control staining (Supplemental Figure S2).

MPIO antibody loading and *in vitro* binding ability were initially assessed for three commercially available anti-mouse ALCAM antibodies (Supplemental Figure S3). Antibody loading densities were calculated to be 23,657 ± 3,128 ALCAM (R&D systems), 17,735 ± 1,429 ALCAM (LSBio), 18,263 ± 5,181 ALCAM (eBio) and 18,985 ± 4,230 IgG antibodies per MPIO (mean ± SD, n = 10 per group). These densities are equivalent to 13,000, 9,700, 10,000 ALCAM (R&D systems, LSBio, and eBio, respectively) and 10,500 IgG antibodies per μm² surface of MPIO (diameter: 0.76 μm).

Binding capacities of conjugates were first assessed under static conditions. TNF stimulated sEnd-1 cells showed marked ALCAM expression (Supplemental Figure S3 and Figure 1), and the percentage of MPIO (red) that co-localised with ALCAM (green) for each FoV was quantified. The R&D antibody conjugate was found to have significantly higher ($p < 0.05$) binding to ALCAM on sEnd-1 cells than LSBio, eBio and IgG antibody conjugates (Figure 1(a) to (c) and Supplemental Figure S3(B) and (C)).

Based on the above results, all subsequent experiments were carried out using the monoclonal rat anti-mouse ALCAM antibody purchased from R&D Systems. Binding to ALCAM-coated capillaries under flow was significantly ($p < 0.001$) greater than either IgG-MPIO, or ALCAM-MPIO binding to BSA-coated capillaries (n = 10 FoV; Figure 1(d) to (g)). The sheer stress induced by the flow of 20–25 μl.min⁻¹ in these capillaries would be comparable to the shear stress experienced within arterioles *in vivo*.[27]

Assessment of ALCAM expression in breast, melanoma and lung brain metastasis models

To assess the suitability of the three brain metastasis models for proof-of-principle ALCAM-targeted imaging *in vivo*, upregulation of ALCAM was first assessed immunohistochemically. Brain metastases were detected
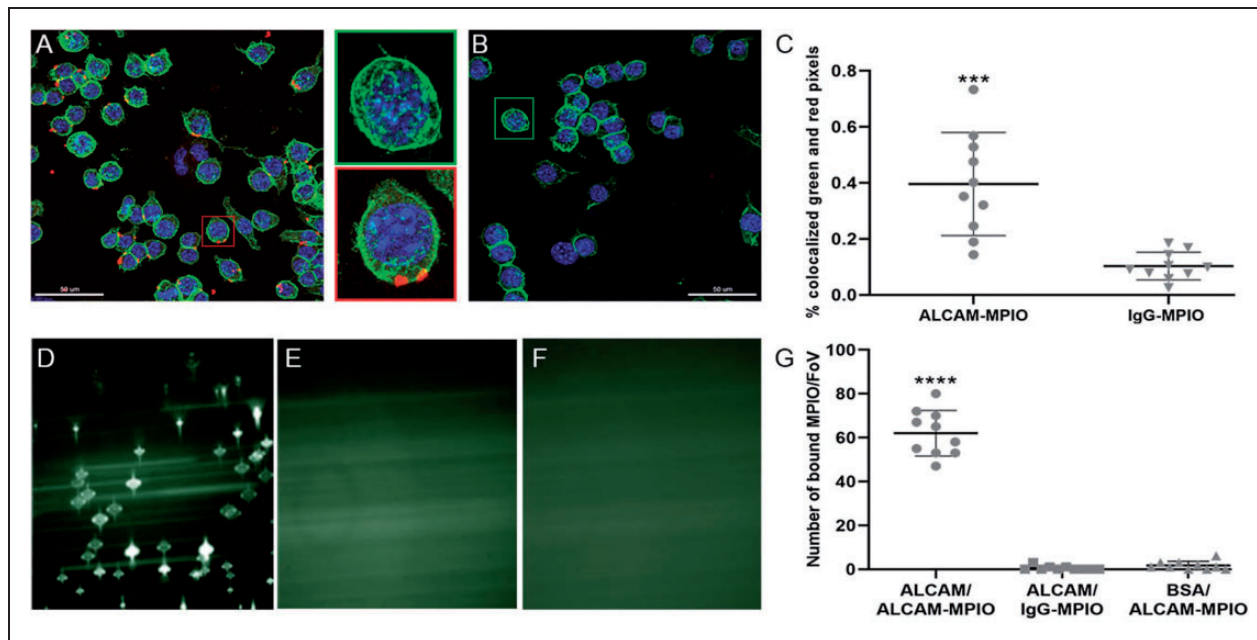
Figure 1. ALCAM-MPIO construct and its binding ability in vitro. (a–c) Immunofluorescent images showing binding of R&D ALCAM-MPIO (red box) (a) or IgG-MPIO (green box) (b) on TNF stimulated mouse endothelial cells; red = MPIO, green = ALCAM and blue = DAPI. Scale bars = 10 μm. (c) Graph showing percentage of co-localized red (MPIO) and green (ALCAM) pixels for each FoV; R&D ALCAM-MPIO showed significantly higher binding to endothelial cell ALCAM than IgG-MPIO; ***$p < 0.001$. (d–g) Fluorescently labelled ALCAM-MPIO (d) or IgG-MPIO (e) were pumped through glass capillaries coated with ALCAM protein, or ALCAM-MPIO were pumped through glass capillaries coated with control BSA protein (f). Only binding of ALCAM-MPIO to ALCAM coated capillaries was evident (d). (g) Graph showing number of ALCAM- or IgG-MPIO bound to the capillary wall; ALCAM-MPIO binding to ALCAM coated capillaries was significantly higher than either IgG-MPIO in ALCAM coated capillaries or ALCAM-MPIO in BSA coated capillaries. ****$p < 0.0001$.

histologically in all mice following successful intracardiac tumor cell injection. In both MDA231Br-GFP and H1_DL2 models, ALCAM expression was evident from the earliest stages of tumor formation (Supplemental Figure S4(A) and (B)). Similarly, ALCAM expression was found in mice injected with SEBTA-001 cells at both time-points studied (Supplemental Figure S4(C)). No ALCAM expression was found in naïve mouse brain (Supplemental Figure S4(D)), in accord with previously published data.[17] Quantitation of ALCAM immunohistochemical staining showed an increase in the overall number of ALCAM positive pixels, irrespective of cell origin and cell type, with tumour progression. However, when the number of ALCAM positive pixels was normalized by tumor area (% ALCAM+), consistent (33–41%) expression was evident throughout the time-course for all three brain metastasis models (Supplemental Figure S4(E)).

Although the above analysis indicated upregulation of ALCAM in all three models, the specific cellular target for this study is endothelial ALCAM. Therefore, to assess temporal expression of ALCAM on vessels, co-localization of ALCAM and the endothelial marker CD31 was assessed immunofluorescently (Figure 2(a) to (c)). Two subsets of vessels were evaluated: (i) intra-tumoral vessels, in close association with tumor cells; and (ii) peri-tumoral vessels, 20–100 μm away from tumor cells. In the MDA231Br-GFP model, a substantial percentage of intra-tumoral vessels were positive for ALCAM (% ALCAM+) and this percentage increased significantly from day 7 to 21 ($p < 0.01$; Figure 2(d)). As the H1_DL2 metastases grow slower than the MDA231Br-GFP metastases and only a few tumors were detectable at day 7, ALCAM/CD31 co-localization was assessed from day 14 in this model. In H1_DL2 model, intra-tumoral vessels showed elevated and stable ALCAM expression across the time-course, with no significant differences between time-points (Figure 2(e)). A similar pattern was observed in the SEBTA-001 model (Figure 2(f)), with ALCAM positive intra-tumoral vessels at both days 35 and day 42 after tumor cell injection. As for the ALCAM expression on peri-tumoral vessels, only MDA231Br-GFP showed a significant increase at days 21 and 28 post tumour injection ($p < 0.05$; Figure 2(g)). No significant difference was found in ALCAM expression on peri-tumoral vessels at any time-point
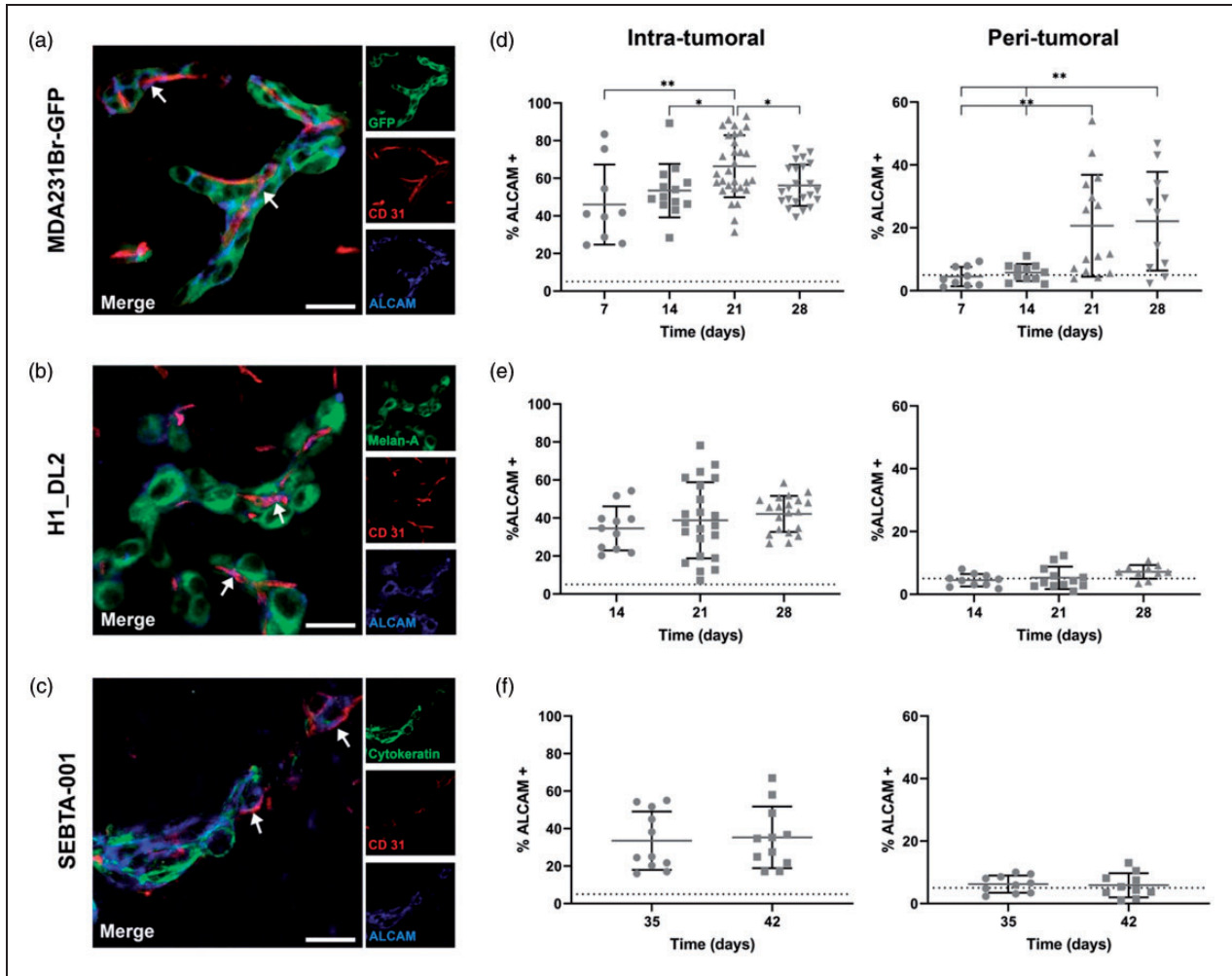
Figure 2. ALCAM/CD31 co-localization in mouse brain metastases from breast, melanoma and lung. (a–c) Representative immunofluorescence images of brain metastases from MDA231Br-GFP (GFP, green), H1_DL2 (Melan-A, green) and SEBTA-001 (cytokeratin, green) showing co-localization (white arrows) of ALCAM (blue) expressed on mouse cerebrovascular cells (CD31, red) at day 21 (MDA231Br-GFP and H1_DL2) and day 42 (SEBTA-0001) models, respectively, post-tumor cell injection. Scale bars = 25μm. (d–f) Graphs showing quantitative analysis of the percentage of ALCAM positive intra-tumoral vessels for the MDA231Br-GFP, H1_DL2 and SEBTA-001 models, respectively. (g–i) Graphs showing quantitative analysis of the percentage of ALCAM positive peri-tumoral vessels for the MDA231Br-GFP, H1_DL2 and SEBTA-001 models, respectively. Dotted line = averaged baseline level of ALCAM on normal brain vessels of contralateral hemisphere. $*p < 0.05$, $**p < 0.01$; $n > 15$ tumors per group.

compared to baseline levels for H1_DL2 and SEBTA-001 models (Figure 2(h) and (i)). Thus, this immunofluorescent co-localization analysis indicates that as tumours grow, the absolute number of ALCAM positive vessels increases, since the total number of intratumoral vessels increases with tumour growth, and to an even greater degree in the breast cancer brain metastases model.

In vivo detection of breast, melanoma and lung brain micrometastases using ALCAM-MPIO

Negligible hypointense foci were detected in control naïve mice injected with MPIO, IgG-MPIO or ALCAM-MPIO (Figure 3(a)), or in tumor bearing cohorts injected with IgG-MPIO (Figure 3(b)). Mice bearing breast, melanoma and lung brain metastases were injected intravenously with either ALCAM-MPIO or control IgG-MPIO at days 21 and 28 (breast and melanoma) or day 42 (lung) post-tumor cell injection. In all cases, T_2*-weighted MGE3D images showed marked hypointensities arising from bound ALCAM-MPIO. Focal hypointense areas were evident throughout the brain for all three models (Figure 4(a); arrows). Quantitation of the number of hypointense voxels in each brain showed a significant difference between mice injected with ALCAM-MPIO and IgG-MPIO for all tumor models and at all time-
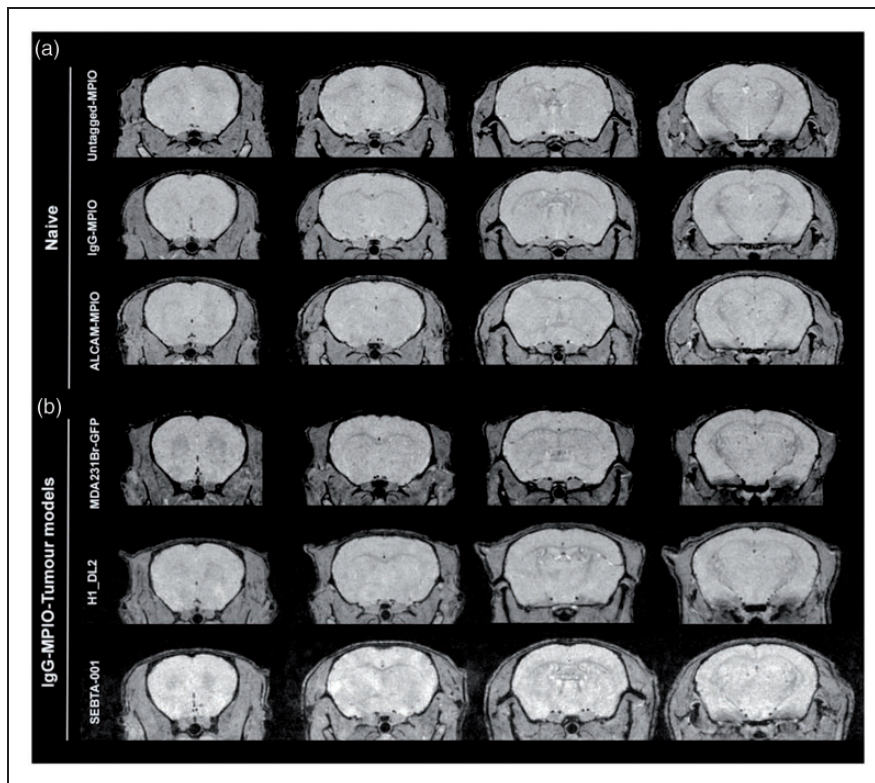
Figure 3. ALCAM-MPIO specificity assessment in naïve mice. (a) Representative T_2*-weighted MGE3D coronal images from naïve mice injected with either (i) untagged ProMag^{TM} carboxylic MPIO, (ii) IgG-MPIO, or (iii) ALCAM-MPIO. Negligible hypointense voxels arising from MPIO were detected in these control group. (b) Representative T_2*-weighted MGE3D coronal images from tumour bearing mice injected with non-specific IgG-MPIO on day 21 (MDA231Br-GFP, H1_DL2) and day 42 (SEBTA-001). Again, minimal hypointense voxels were detected in these mice.

points studied (Figure 4(b)). For all tumor bearing mice, no signal enhancement was seen on conventional gold standard post-gadolinium T_1-weighted images, confirming an intact BBB (Figure 5).

Histological detection of metastases remains the gold standard currently, and examination of mice injected with either ALCAM-MPIO or IgG-MPIO showed the presence of widespread brain metastases for all models. The majority of hypointensities on T_2*-weighted MGE3D images corresponded spatially with micrometastases detected histologically (arrows, Figure 6(a) to (i)) in all three brain metastasis models. Presence of both MPIO (iron staining) and endothelial ALCAM on vessels in close proximity to brain metastases was evident (Figure 6(j) to (l)).

Classification accuracy of ALCAM-MPIO imaging in metastasis models

To assess the accuracy of ALCAM-MPIO MRI, both the number of metastases associated with vascular ALCAM positivity, and the number of brain metastases detected by ALCAM-MPIO MRI were first determined. For the MDA231Br-GFP, H1_DL2, and SEBTA-001 models, 89%, 51% and 79% of all metastases had ALCAM positive vessels, respectively (n = 3 mice; Table 1). By manually correlating the anatomical location of brain metastases on histology with the corresponding hypointensities on T_2*-weighted images, it was determined that that 82%, 55% and 68% of all metastases were detected by ALCAM-MPIO MRI for the MDA231Br-GFP, H1_DL2, and SEBTA-001 model, respectively (Table 1(A) to (C)). When considering just the metastases with ALCAM-positive vessels determined histologically, the sensitivity for their detection with ALCAM-MPIO MRI was 90%, 85% and 80% in MDA231Br-GFP, H1_DL2 and SEBTA-001 models, respectively, whilst the corresponding specificities were 83%, 76% and 79%, respectively. If all animals were combined, overall sensitivity was 86% and specificity was 78% ($p < 0.001$ in all cases, Fisher's exact test). Full classification summary statistics are given in Table 1(D). Classification results were similar for both large and small tumours within each cell line (Supplementary Tables S1 and S2, respectively).
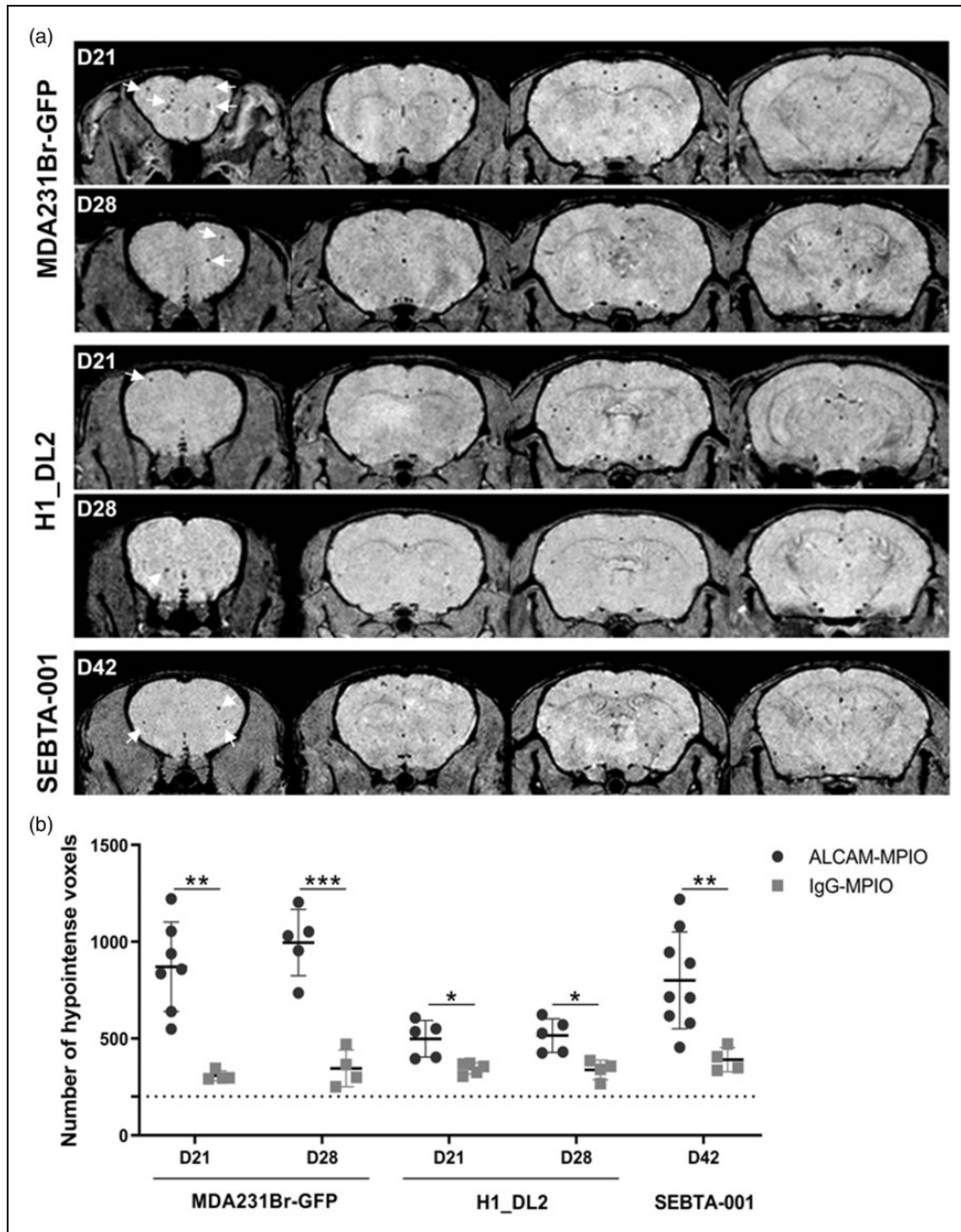
Figure 4. Detection of brain micrometastases using ALCAM-MPIO. (a) Representative T_2*-weighted coronal images from MGE3D datasets. Prominent focal hypointense (black) foci corresponding to retention of ALCAM-MPIO were evident in mice injected with MDA231Br-GFP or H1_DL2 cells at both days 21 and 28, and SEBTA-001 cells at day 42. Examples of hypointense foci are indicated with white arrows in the first column. (b) Graph showing quantitation of the number of hypointense voxels for each tumor model (n = 4–8 per group). A significant difference was evident between tumor bearing mice injected with ALCAM-MPIO (black circles) and IgG-MPIO (grey squares) for all time-points in all three models; *$p < 0.05$, **$p < 0.01$, ***$p < 0.001$. Dashed line denotes background hypointense voxels detected in naive mice injected with ALCAM-MPIO (n = 2).

Assessment of ALCAM expression in human brain metastasis biopsies

In all cases studied, immunohistochemistry of human brain biopsies showed high expression of ALCAM on vessels adjacent to metastases from breast, melanoma and lung (n ≥ 3 cases for each primary; Supplemental Figure S5). Expression of ALCAM was also evident on many tumor cells, but to differing degrees dependent on primary tumor type. Both negative control staining and control, healthy brain tissue showed no ALCAM positivity (Supplemental Figure S5(G) and (H)).
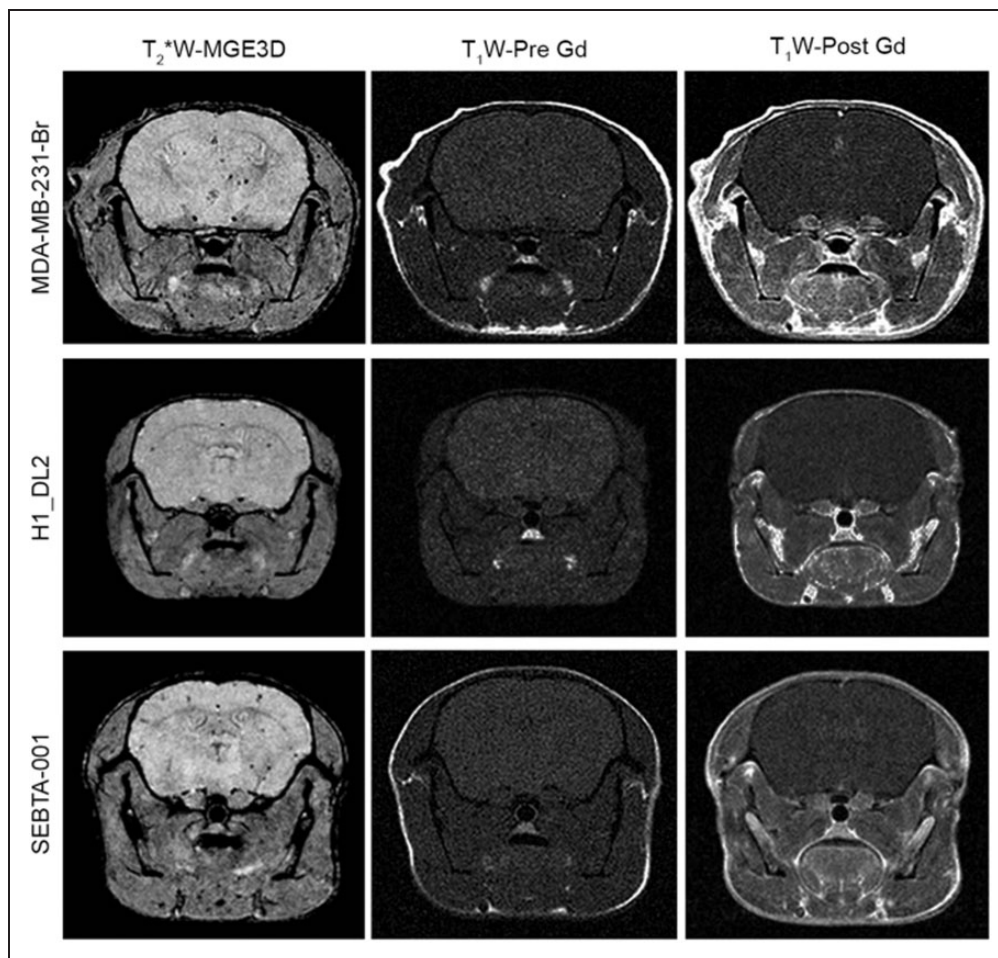
Figure 5. MRI BBB permeability assessment in the brain metastasis models. (Top three rows) Representative T_2*-weighted MGE3D images and corresponding gold standard T_1-weighted pre- and post-gadolinium images for mice injected intracardially with MDA-MB-231-Br, H1_DL2 or SEBTA-001 cells. No gadolinium enhancement (bright regions) was detected in T_1-weighted post-Gd images, indicating an intact BBB. The presence of hypointense foci on the T_2*-weighted MGE3D correspond to the bound ALCAM-MPIO and micrometastases, which are not detected on the post-contrast T_1-weighted image. Images are from the latest time-point of the study (day 28 post-injection for MDA-MB-231-Br, H1_DL2 and day 42 for SEBTA-001).

Discussion

In this study, we report the development and implementation of a novel MRI molecular imaging agent targeting activated leukocyte cell adhesion molecule (ALCAM). We first demonstrate that this new agent shows high selectivity and sensitivity for ALCAM targeting *in vitro*. Subsequently, in a proof-of-concept study, we show that the agent enables detection of endothelial ALCAM expression *in vivo* in mouse models of brain micrometastasis originating from breast, melanoma and lung primary cancers.

Inflammation is a key component of the pathophysiology of most neurological disorders, including cancer. Adhesion molecules play an important role in the inflammatory process and assist with trafficking of leukocytes from the bloodstream to the brain

across the BBB. Recently, ALCAM has been reported to play an important role in this process and its upregulation on the brain vasculature has been shown to correlate with pathogenesis and disease progression in MS,[13,15,16,28] stroke[29] and cancer.[17] The specificity of ALCAM to disease site, and accessibility of this biomarker on the vascular endothelium, makes it a potentially important target for molecular imaging and targeted therapy. Therefore, in this study, our aim was to develop a novel anti-ALCAM MRI contrast agent for *in vivo* detection of endothelial ALCAM upregulation in neuroinflammatory conditions.

First, the optimal anti-mouse ALCAM antibody for targeted MPIO construct was identified and tested. Anti-ALCAM antibody density levels on MPIO from R&D Systems ($\sim$23,000 Ab/MPIO) was comparable
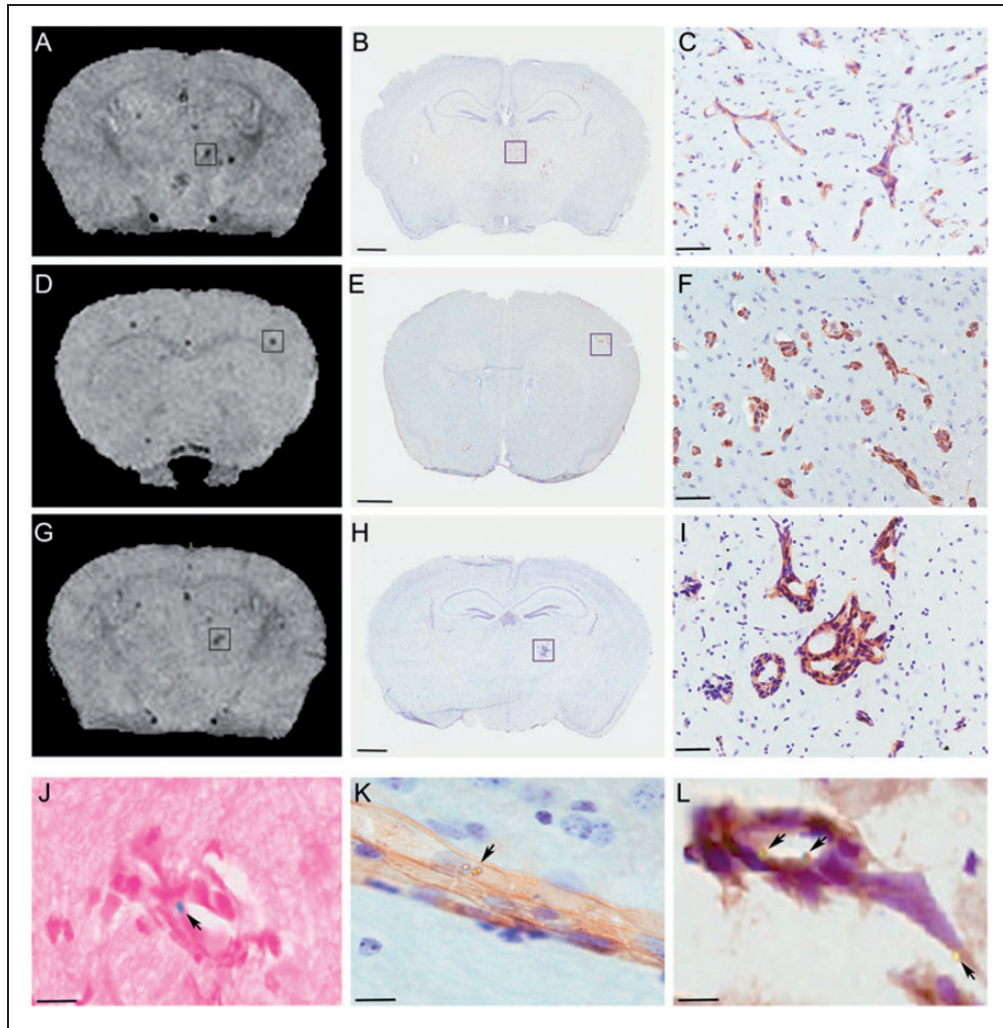
Figure 6. ALCAM-MPIO binding and detection of brain metastases. (a–c) Representative T_2*-weighted MGE3D image from MDA-MB-231-Br brain metastasis model and the corresponding histological section (b) showing an example of co-localisation of hypo-intensities on the T_2*-weighted image with brain metastases (boxes) and (c) the higher magnification photomicrograph from ALCAM (brown) stained tumour. Counterstain = cresyl violet; blue. (d–f) Representative T_2*-weighted MGE3D image from the H1_DL2 brain metastasis model and the corresponding histological sections. (g–i) Representative T_2*-weighted MGE3D image from SEBTA-001 brain metastasis model and the corresponding histological sections. (j) Perls' Prussian blue staining of tumour showing presence of MPIO (blue; arrows), counterstain = Nuclear Fast Red. (k and l) MPIO (black arrows) were found in ALCAM activated vessels (brown); nuclei of tumour cells are evident in close association with ALCAM-positive vessels. Scale bars: (b, e, h) = 1 mm; (c, f, l, j) = 30 μm; (e, f) = 5 μm.

with previously published data for other antibody-targeted MPIO such as VCAM-1, E-selectin and PECAM-1 (20,000–27,000 Ab/MPIO).[11,20,27] The optimal ALCAM-MPIO conjugate showed marked binding to ALCAM expressed on cytokine-stimulated mouse endothelial cells *in vitro* and target specificity was confirmed under flow condition in glass capillaries pre-coated with the recombinant ALCAM protein compared to those pre-coated with BSA. Similar binding patterns and specificity of binding have previously been demonstrated by McAteer et al. for VCAM-1 targeted MPIO.[30]

We next demonstrated that ALCAM-targeted imaging enables sensitive and specific detection of endothelial ALCAM expression *in vivo*. For this proof-of-concept study, we used three different mouse models of secondary brain cancer, metastasis, from the three primary tumour types with the highest incidence of brain metastases. We have previously demonstrated upregulation of endothelial ALCAM in early breast cancer brain metastasis,[17] and this was further confirmed here across a longer time-frame and extended to models of lung and melanoma brain metastasis. Although ALCAM expression as a percentage of

Table 1. Classification accuracy of ALCAM-MPIO imaging in metastasis models.

A. MDA231Br-GFP (breast cancer primary)

		Histological endothelial ALCAM	
		+	−
Hypointensity on ALCAM-MPIO MRI	+	84	2
	−	9	10

B. H1_DL2 (melanoma primary)

		Histological endothelial ALCAM	
		+	−
Hypointensity on ALCAM-MPIO MRI	+	33	9
	−	6	29

C. SEBTA-001 (non-small cell lung cancer primary)

		Histological endothelial ALCAM	
		+	−
Hypointensity on ALCAM-MPIO MRI	+	57	4
	−	14	15

D. Statistical summaries

	MDA231BR-GFP	H1_DL2	SEBTA-001	All tumours
Sensitivity				
Chance of a histologically ALCAM positive tumour being identified by ALCAM-MRI	0.903	0.846	0.803	0.857
Specificity				
Chance of an MRI negative tumour also being histologically ALCAM negative	0.833	0.763	0.789	0.783
Accuracy				
Overall chance of MRI classification matching histological classification	0.895	0.805	0.800	0.838
Prevalence				
Overall chance of a tumour being histologically ALCAM positive	0.737	0.506	0.789	0.746
Fisher's exact test p-value	1.7×10^{-7}	5.3×10^{-8}	2.8×10^{-6}	0

(A–C) 2×2 contingency tables showing the number of tumours that were identified as positive or negative by either endothelial ALCAM histology or by ALCAM-MPIO MRI in the three cell lines. (D) Table of statistical summaries identifying how good ALCAM-MPIO MRI was at detecting known histologically ALCAM-positive tumours (sensitivity, also known as true positive rate), how likely it was that a tumour that was not positive on ALCAM-MPIO MRI was actually ALCAM negative by histology (specificity, also known as true negative rate), how likely it was that the ALCAM-MPIO MRI matched the histological observation (accuracy), how likely it was that any given tumour was ALCAM positive by histology (prevalence), and the Fisher's exact test p-value for the classification.

tumour volume appeared to be stable across the time courses studied for all models, specific endothelial ALCAM expression showed a progressive upregulation on intra-tumoral vessels over time in the breast cancer brain metastasis model, together with upregulation of ALCAM on peri-tumoral vessels (up to *ca*.100 μm away from metastatic cells) at later time-points. For the melanoma and lung brain metastasis models, the percentage of intra-tumoral vessels showing upregulation of endothelial ALCAM appeared to be stable across all time-points studied. Thus, these models provide an appropriate test system for this proof-of-concept study.

In the breast cancer brain metastasis model, at day 21, a significant proportion (82%) of brain metastases found histologically co-registered with hypointensities on T_2*-weighted images. This finding was in accord with the percentage of tumors that showed endothelial ALCAM positivity (89%). ALCAM-MPIO detection was evident across the range of tumor volumes observed, with no clear threshold for detection; the smallest breast cancer brain metastasis that was detected was approximately 7.8×10^{-5} μl in volume. In the melanoma model, ALCAM-MPIO appeared to detect fewer metastases (55%). However, the histological results also showed that endothelial ALCAM

upregulation was present in a similar percentage of tumors (51%), in support of the *in vivo* findings. Similarly, in the lung cancer brain metastasis model, ALCAM-MRI enabled detection of 68% of all tumors, with 79% showing endothelial ALCAM expression. Critically, when considering only the metastases showing endothelial ALCAM upregulation histologically, 90%, 85% and 80% of these tumours were detected using ALCAM-targeted MRI in breast, melanoma and lung brain metastases models, respectively. In each cell line, a small number of tumours were identified by ALCAM-targeted MRI that were not confirmed as histologically ALCAM-positive (2%, 12% and 4% for breast, melanoma and lung, respectively). These apparent false positives, however, may reflect the mismatch between MRI and histology resolutions and endothelial ALCAM expression may have been present in an unstained section. Together, these data indicate high specificity and sensitivity of the ALCAM-MPIO for detection of endothelial ALCAM upregulation on the cerebral vasculature *in vivo*.

Although, owing to their size, MPIO are considered to be obligate intravascular agents even in the presence of a compromised BBB, in order to confirm specific endoluminal binding of a novel contrast agent *in vivo*, it is essential to use a model in which the BBB remains intact. In this case, the possibility of accumulation within the brain across a permeable BBB can be definitively excluded. In the models used here, we demonstrated the presence of an intact BBB with post-gadolinium T_1-weighted MRI, at each of the time-points studied, thus indicating specific endoluminal binding of the ALCAM-MPIO. Subsequent immunohistochemical and immunofluorescent analysis of tissue *ex vivo* confirmed the endoluminal presence of ALCAM-MPIO adjacent to ALCAM-expressing endothelium and in close proximity to micrometastases.

Currently, MRI diagnosis of brain metastases relies on extravasation of gadolinium from the circulation into the tumor microenvironment. Metastases need to reach a minimum size of *ca*.2 mm in diameter before they become visible on MRI.[31,32] Although MRI is highly sensitive for tumors with a disrupted BBB, permeability of brain metastases to contrast agents has been shown to be heterogeneous.[33,34] Moreover, in the micrometastatic stages the BBB remains completely impermeable,[20,22] masking these tumors from detection by contrast-enhanced MRI. In the models used here, the micrometastases detected using ALCAM-targeted MRI were considerably smaller than this size threshold for detection, and did not have a permeable BBB, as demonstrated by post-gadolinium T_1-weighted MRI. To note, these micrometastases are also not detectable by conventional T_1- or T_2-weighted anatomical imaging (Supplemental Figure S6). These data suggest that

ALCAM-targeted molecular imaging may enable earlier detection of brain micrometastases, prior to BBB breakdown.

ALCAM expression in human tissue has been explored previously in a number of malignancies,[35–39] including, very recently, lung cancer brain metastasis.[18] Moreover, Wu *et al* have reported the development of a human anti-ALCAM PET tracer, which was able to target and detect human pancreatic adenocarcinoma and colorectal carcinoma in xenograft mouse models.[40,41] In all of those studies, however, the focus was on expression of ALCAM on tumour cells, rather than the vascular endothelium. Whilst tumour cell ALCAM is accessible in many tumours where the vasculature is leaky, the presence of an intact BBB, either entirely or partially, can preclude access of imaging agents to brain tumours. Consequently, the presence of ALCAM on cerebral vessels is particularly important for the development of neurological diagnostic probes. Here, we have shown that ALCAM is expressed on tumor-associated blood vessels in all human brain metastasis samples studied, independent of the primary origin (breast, melanoma or lung), whilst ALCAM expression distant from tumours and in healthy brain tissue was negligible. Whilst these results support the potential of our novel ALCAM-MPIO agent for clinical translation, direct comparison with our previous work using a VCAM-1 targeted contrast agent in the same mouse brain metastasis models[20,22] suggests that VCAM-1 targeted MRI remains the method of choice for early detection of brain micrometastases specifically (Supplementary Table S3). The advantage of VCAM-1-targeted MRI largely reflects the slightly greater percentage of VCAM-1 positive metastases, compared to ALCAM-positive metastases, found in the lung and melanoma brain metastasis models. In addition, a lack of peritumoural spread of the ALCAM signal in the melanoma and lung brain metastasis models yields a more restricted ALCAM-target for the *in vivo* imaging. A possible explanation, for both the lower percentage of ALCAM-positive tumours and minimal per-tumoral spread in the lung and melanoma models compared to the breast cancer brain metastasis model, may be differences in growth patterns, vascular density and angiogenic properties of the models. Co-registration of histology and MRI in the melanoma brain metastasis model, in particular, indicated that ALCAM-MPIO were able to detect the subset of micrometastases that were highly vascular and co-optive in growth pattern, but not those exhibiting a lobular, non co-optive growth pattern (Supplemental Figure S7). In accord with this notion, different phenotypes of growth and interaction with the BBB have been shown previously, depending on the primary origin of brain metastasis

cells.[42,43] Moreover, differences in doubling times of the different cell lines yielded substantially different median volumes for the MDA-MB-231-Br and H1_DL2 models even at the same time-point post-tumour cells injection (day 21; 0.893×10^{-3} µl *vs.* 0.304×10^{-3} µl, respectively) and this may further contribute to the differences in endothelial ALCAM expression observed.

It is well known that not all adhesion molecules are equal and, therefore, being able to image different CAMs *in vivo* will greatly expand our ability not only to determine their roles in different diseases, but also to stratify patient treatment. At the same time, the potential of CAMs as biomarkers for treatment monitoring has yet to be evaluated. Interestingly, others have shown that levels of P-selectin, another adhesion molecule, correlate with tumour progression.[44] Thus, given the differences between the different CAMs in terms of expression profile and function, it is possible that an agent combining VCAM-1, ALCAM and even P-selectin targeting may further improve sensitivity, provide indications of tumour stage and/or enable treatment stratification. Similarly, assessing VCAM-1 and ALCAM expression in macrometastases, where the BBB is only heterogeneously permeable, may reveal differences that could be exploited. Importantly, ALCAM has been shown to be upregulated on the cerebrovascular endothelium in several other neuroinflammatory diseases, including EAE,[15] MS[16] and stroke,[29] and its role in leukocyte recruitment across the BBB is becoming clearer. Thus, based on that literature and the results of the current study, we speculate that our novel agent could be used to detect ALCAM upregulation in a range of neurological diseases.

In conclusion, this study has shown that ALCAM-targeted MRI enables sensitive and specific detection of endothelial ALCAM expression both *in vitro* and *in vivo*. Identifying immunological biomarkers and developing tools such as ALCAM-MPIO potentially enables identification of molecular changes that may drive the development of new immunotherapy drugs. Moreover, combination of this novel imaging agent with relevant therapeutics, to yield a theranostic agent, could enable delivery of drugs and radioactive substances very specifically to disease sites, as already demonstrated for VCAM-1 targeted alpha-particle therapy.[45] The novel ALCAM targeted MRI contrast agent described here could potentially be used in a wide range of neuroinflammatory diseases, including MS, stroke and cancer, where its presence has been shown to be key for the extravasation of leukocyte across endothelial cells. Although the resolution achievable in mice is considerably higher than is currently possible clinically, previous calculations have shown that MPIO signal reduction should be detectable with clinical approaches.[22] With the recent development of a biodegradable multimeric MPIO (mMPIO),[19] clinical translation of novel imaging agents, such as ALCAM-MPIO, is a realistic possibility.

Declaration of conflicting interests

The author(s) declared no potential conflicts of interest with respect to the research, authorship, and/or publication of this article.

Authors' contributions

Experimental design: NZ, MSS, NRS. Acquisition and analysis/interpretation of data: NZ, AAK, CSK, VAJ, OA, JRL. Provision of human biopsy samples: OA. Development of novel contrast agent: NZ, FPB. Drafting of manuscript: NZ, NRS. Manuscript revision: MSS, FPB, AAK, VAJ, OA, JRL.

Supplementary material

Supplemental material for this article is available online.

ORCID iDs

Niloufar Zarghami https://orcid.org/0000-0001-8520-9660
Alexandre A Khrapitchev https://orcid.org/0000-0002-7616-6635
James R Larkin https://orcid.org/0000-0002-4169-8447

References

1. Fung A, Vizcaychipi M, Lloyd D, et al. Central nervous system inflammation in disease related conditions: mechanistic prospects. *Brain Res* 2012; 1446: 144–155.
2. Muller WA. Getting leukocytes to the site of inflammation. *Vet Pathol* 2013; 50: 7–22.
3. Gauberti M, Montagne A, Quenault A, et al. Molecular magnetic resonance imaging of brain-immune interactions. *Front Cell Neurosci* 2014; 8: 389.

4. Gauberti M, Fournier AP, Docagne F, et al. Molecular magnetic resonance imaging of endothelial activation in the Central nervous system. *Theranostics* 2018; 8: 1195–1212.

5. Serres S, Mardiguian S, Campbell SJ, et al. VCAM-1-targeted magnetic resonance imaging reveals subclinical disease in a mouse model of multiple sclerosis. *Faseb J* 2011; 25: 4415–4422.

6. Montagne A, Gauberti M, Macrez R, et al. Ultra-sensitive molecular MRI of cerebrovascular cell activation enables early detection of chronic central nervous system disorders. *Neuroimage* 2012; 63: 760–770.

7. Mardiguian S, Serres S, Ladds E, et al. Anti-IL-17A treatment reduces clinical score and VCAM-1 expression detected by in vivo magnetic resonance imaging in chronic relapsing EAE ABH mice. *Am J Pathol* 2013; 182: 2071–2081.

8. Blezer ELA, Deddens LH, Kooij G, et al. *In vivo* MR imaging of intercellular adhesion molecule-1 expression in an animal model of multiple sclerosis. *Contrast Media Mol Imaging* 2015; 10: 111–121.

9. Fournier AP, Quenault A, De Lizarrondo SM, et al. Prediction of disease activity in models of multiple sclerosis by molecular magnetic resonance imaging of P-selectin. *Proc Natl Acad Sci U S A* 2017; 114: 6116–6121.

10. Quenault A, De Lizarrondo SM, Etard O, et al. Molecular magnetic resonance imaging discloses endothelial activation after transient ischaemic attack. *Brain* 2017; 140: 146–157.

11. Zarghami N, Khrapitchev AA, Perez-Balderas F, et al. Optimization of molecularly targeted MRI in the brain: empirical comparison of sequences and particles. *Int J Nanomed* 2018; 13: 4345–4359.

12. Masedunskas A, King JA, Tan F, et al. Activated leukocyte cell adhesion molecule is a component of the endothelial junction involved in transendothelial monocyte migration. *FEBS Lett* 2006; 580: 2637–2645.

13. Lyck R, Lécuyer MA, Abadier M, et al. ALCAM (CD166) is involved in extravasation of monocytes rather than T cells across the blood–brain barrier. *J Cereb Blood Flow Metab* 2017; 37: 2894–2909.

14. Samaha H, Pignata A, Fousek K, et al. A homing system targets therapeutic T cells to brain cancer. *Nature* 2018; 561: 331–337.

15. Lécuyer MA, Saint-Laurent O, Bourbonnière L, et al. Dual role of ALCAM in neuroinflammation and blood-brain barrier homeostasis. *Proc Natl Acad Sci U S A* 2017; 114: E524–E533.

16. Michel L, Grasmuck C, Charabati M, et al. Activated leukocyte cell adhesion molecule regulates B lymphocyte migration across central nervous system barriers. *Sci Transl Med* 2019; 11: eaaw0475.

17. Soto MS, Serres S, Anthony DC, et al. Functional role of endothelial adhesion molecules in the early stages of brain metastasis. *Neuro Oncol* 2014; 16: 540–551.

18. Münsterberg J, Loreth D, Brylka L, et al. ALCAM contributes to brain metastasis formation in non-small-cell lung cancer through interaction with the vascular endothelium. *Neuro Oncol* 2020; 22: 955–966.

19. Perez-Balderas F, van Kasteren SI, Aljabali AAA, et al. Covalent assembly of nanoparticles as a peptidase-degradable platform for molecular MRI. *Nat Commun* 2017; 8: 14254.

20. Cheng VWT, Soto MS, Khrapitchev AA, et al. VCAM-1–targeted MRI enables detection of brain micrometastases from different primary tumors. *Clin Cancer Res* 2019; 25: 533–534.

21. Workman P, Aboagye EO, Balkwill F, et al.; An ad hoc committee of the National Cancer Research Institute. Guidelines for the welfare and use of animals in cancer research. *Br J Cancer* 2010; 102: 1555–1557.

22. Serres S, Soto MS, Hamilton A, et al. Molecular MRI enables early and sensitive detection of brain metastases. *Proc Natl Acad Sci* 2012; 109: 6674–6679.

23. Jassam SA, Maherally Z, Smith JR, et al. CD15s/CD62E interaction mediates the adhesion of non-small cell lung cancer cells on brain endothelial cells: Implications for cerebral metastasis. *Int J Mol Sci* 2017; 18: 1–16.

24. Gilchrist S, Gomes AL, Kinchesh P, et al. An MRI-compatible high frequency AC resistive heating system for homeothermic maintenance in small animals. *PLoS One* 2016; 11: e0164920.

25. Yushkevich PA, Piven J, Hazlett HC, et al. User-guided 3D active contour segmentation of anatomical structures: significantly improved efficiency and reliability. *Neuroimage* 2006; 31: 1116–1117.

26. Hamilton A. *MRI and histological analysis of brain metastasis and the effect of systemic inflammation.* Doctoral dissertation, University of Oxford, UK, 2013.

27. Jefferson A, Wijesurendra RS, McAteer MA, et al. Molecular imaging with optical coherence tomography using ligand-conjugated microparticles that detect activated endothelial cells: Rational design through target quantification. *Atherosclerosis* 2011; 219: 579–587.

28. Wagner M, Bilinska M, Pokryszko-Dragan A, et al. ALCAM and CD6 - multiple sclerosis risk factors. *J Neuroimmunol* 2014; 276: 98–103.

29. Smedbakken L, Jensen JK, Hallén J, et al. Activated leukocyte cell adhesion molecule and prognosis in acute ischemic stroke. *Stroke* 2011; 42: 2453–2458.

30. Mcateer MA, Sibson NR, Mühlen C, Von, et al. In vivo magnetic resonance imaging of acute brain inflammation using microparticles of iron oxide. *Nat Med* 2007; 13: 1253–1258.

31. Nomoto Y, Miyamoto T and Yamaguchi Y. Brain metastasis of small cell lung carcinoma: comparison of gd-dtpa enhanced magnetic resonance imaging and enhanced computerized tomography. *Jpn J Clin Oncol* 1994; 24: 258–262.

32. Mehrabian H, Detsky J, Soliman H, et al. Advanced magnetic resonance imaging techniques in management of brain metastases. *Front Oncol* 2019; 9: 440.

33. Murrell DH, Hamilton AM, Mallett CL, et al. Understanding heterogeneity and permeability of brain metastases in murine models of HER2-positive breast cancer through magnetic resonance imaging: Implications for detection and therapy. *Transl Oncol* 2015; 8: 176–184.

34. Henry MN, Chen Y, McFadden CD, et al. In-vivo longitudinal MRI study: an assessment of melanoma brain metastases in a clinically relevant mouse model. *Melanoma Res* 2015; 25: 127–137.

35. Ofori-Acquah SF and King JA. Activated leukocyte cell adhesion molecule: a new paradox in cancer. *Transl Res* 2008; 151: 122–128.

36. Weidle UH, Eggle D, Klostermann S, et al. ALCAM/CD166: cancer-related issues. *Cancer Genom Proteom* 2010; 244: 231–243.

37. van Kempen LC, van den Oord JJ, van Muijen GN, et al. Activated leukocyte cell adhesion molecule/CD166, a marker of tumor progression in primary malignant melanoma of the skin. *Am J Pathol* 2000; 156: 769–774.

38. Kijima N, Hosen N, Kagawa N, et al. CD166/activated leukocyte cell adhesion molecule is expressed on glioblastoma progenitor cells and involved in the regulation of tumor cell invasion. *Neuro Oncol* 2012; 14: 1254–1264.

39. Devis L, Moiola CP, Masia N, et al. Activated leukocyte cell adhesion molecule (ALCAM) is a marker of recurrence and promotes cell migration, invasion, and metastasis in early-stage endometrioid endometrial cancer. *J Pathol* 2017; 241: 475–487.

40. Tavaré R, Wu WH, Zettlitz KA, et al. Enhanced immunoPET of ALCAM-positive colorectal carcinoma using site-specific 64Cu-DOTA conjugation. *Protein Eng Des Select* 2014; 27: 317–324.

41. McCabe KE, Liu B, Marks J, et al. An engineered cysteine-modified diabody for imaging activated leukocyte cell adhesion molecule (ALCAM)-positive tumors. *Mol Imaging Biol* 2012; 14: 336–347.

42. Kienast Y, Von Baumgarten L, Fuhrmann M, et al. Real-time imaging reveals the single steps of brain metastasis formation. *Nat Med* 2010; 16: 116–122.

43. Carbonell WS, Ansorge O, Sibson N, et al. The vascular basement membrane as 'soil' in brain metastasis. *PLoS One* 2009; 4: e5857.

44. Peeters CFJM, Ruers TJM, Westphal JR, et al. Progressive loss of endothelial P-selectin expression with increasing malignancy in colorectal cancer. *Lab Invest* 2005; 85: 248–256.

45. Corroyer-Dulmont A, Valable S, Falzone N, et al. VCAM-1 targeted alpha-particle therapy for early brain metastases. *Neuro Oncol* 2020; 22: 357–368.